ASSOCIATED CONTENT

Interplay between Composition, Structure and Properties of New H_3PO_4 Doped PBI_4N-HfO_2 Nanocomposite Membranes for High-Temperature Proton Exchange Membrane Fuel Cells

Graeme Nawn[†], *Giuseppe Pace*[†,‡], *Sandra Lavina*[†,§], *Keti Vezzù*[#], *Enrico Negro*[†,§], *Federico Bertasi*[†,§,‡], *Stefano Polizzi*[+,§], *Vito Di Noto*[†,§]*

† Dipartimento di Scienze Chimiche, Università di Padova, Via Marzolo 1, I-35131 Padova (PD), Italy

‡ CNR-IENI, Via Marzolo 1, I-35131 Padova (PD), Italy

§ Consorzio Interuniversitario Nazionale per la Scienza e la Tecnolgia dei Materiali, INSTM, Italy

Veneto Nanotech S.C.p.a., Via San Crispino, 106, I-35129, Padova (PD), Italy

+ Dipartimento di Scienze Molecolari e Nanosistemi, Università di Venezia, Calle Larga S. Marta, Dorsoduro 2137, I-30123 Venezia (VE), Italy

Figure SI-1. Retention of phosphoric acid by composite membranes. Samples were immersed in doubly distilled water at room temperature for 60 minutes before being dried and weighed. $< \alpha >$ is the average percentage of leached phosphoric acid, y and y_{aft} are the number of H_3PO_4 molecules per monomer repeat unit before and after forced leaching respectively

Figure SI-2: TG profiles for PBI4N and $[PBI4N(HfO_2)_x]$ measured under an air atmosphere

Figure SI-3. Weight loss attributed to acid dehydration with increasing nanofiller content observed by TG analysis

Figure SI-4. TG profiles for $[PBI4N(HfO_2)_x](H_3PO_4)_y$ measured under an air atmosphere

Figure SI-5. MDSC profiles for $[PBI4N(H_3PO_4)_x]$ showing heat flow (red) and reversing heat flow (blue)

Figure SI-6. MDSC profiles for $[PBI4N(HfO_2)_x](H_3PO_4)_y$ showing heat flow (red) and reversing heat flow (blue)

Figure SI-7. The effect of nanofiller content (x) on the interplanar distance of (200) and (110) for undoped (circles) and acid-doped (squares) membranes

Figure SI-8. WAXS patter of $[PBI4N(HfO_2)_x]$ (black) and $[PBI4N(HfO_2)_x](H_3PO_4)_y$ (red) with some assigned peaks

Figure SI-9. Temperature dependent storage modulus (*E'*), loss modulus (*E''*) and tan δ profiles for PBI4N and $[PBI4N(HfO_2)_x]$

Figure SI-10. Effect of nanofiller content on the 4 mechanical transitions observed by DMA

Figure SI-11. FT-IR-ATR spectra of all undoped membranes and neat filler

Figure SI-12. FT-IR-ATR spectra of all undoped membranes and neat nanofiller showing assigned in-plane and out-of-plane bands

Figure SI-13. Effect of nanofiller levels on the in-plane vibrational bands of [PBI4N(HfO_2)$_x$] occurring at 1439 cm^{-1} (circles) and 1421 cm^{-1} (squares). The areas under the bands are compared with that of the area under the band occurring at 1528 cm^{-1} which is shown to be largely unaffected by nanofiller content

Figure SI-14. Effect of nanofiller levels on the out-of plane bands of [PBI4N(HfO_2)$_x$] occurring at 792 cm^{-1} (triangles) and 684 cm^{-1} (circles) and 458 cm^{-1}(squares). The areas under the bands are compared with that of the area under the band occurring at 1528 cm^{-1} which is shown to be largely unaffected by nanofiller content

Figure SI-15. FT-IR-ATR spectra of all undoped membranes showing the diminishing intensity of the peak at 458 cm^{-1} with increasing nanofiller content

Figure SI-16. FT-IR-ATR spectra of all acid-doped membranes and *o*-phosphoric acid (85 %)

Figure SI-17. Decomposition of the experimental normalized FT-IR-ATR spectra for acid-doped PBI4N (black) confirming the presence of H_3PO_4 (red) and $H_2PO_4^-$ (blue)

Figure SI-18. Full FT-IR-ATR assignment of PBI4N(HfO_2)$_x$ and [PBI4N(HfO_2)$_x$](H_3PO_4)$_y$

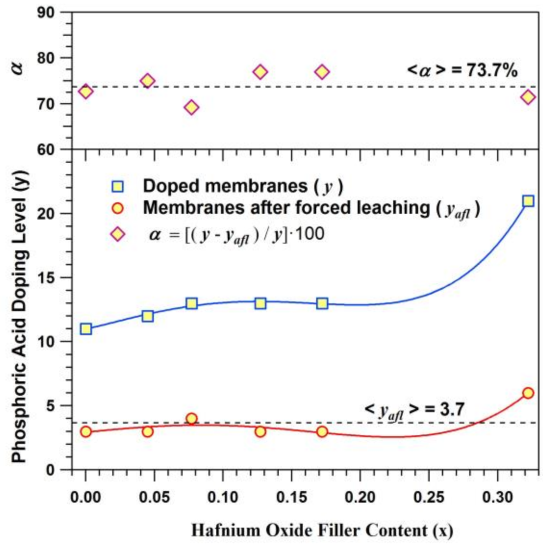

Figure SI-1. Retention of phosphoric acid by composite membranes. Samples were immersed in doubly distilled water at room temperature for 60 minutes before being dried and weighed. < α > is the average percentage of leached phosphoric acid, y and y_{aft} are the number of H_3PO_4 molecules per monomer repeat unit before and after forced leaching respectively

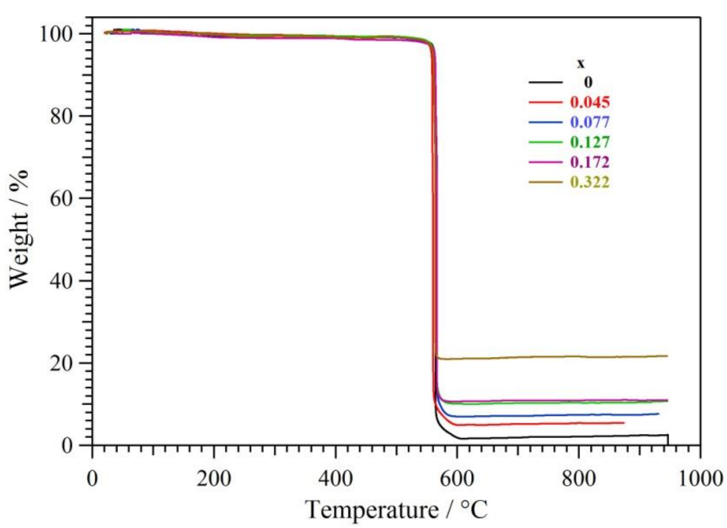

Figure SI-2. TG profiles for PBI4N and [PBI4N(HfO_2)$_x$] measured under an air atmosphere

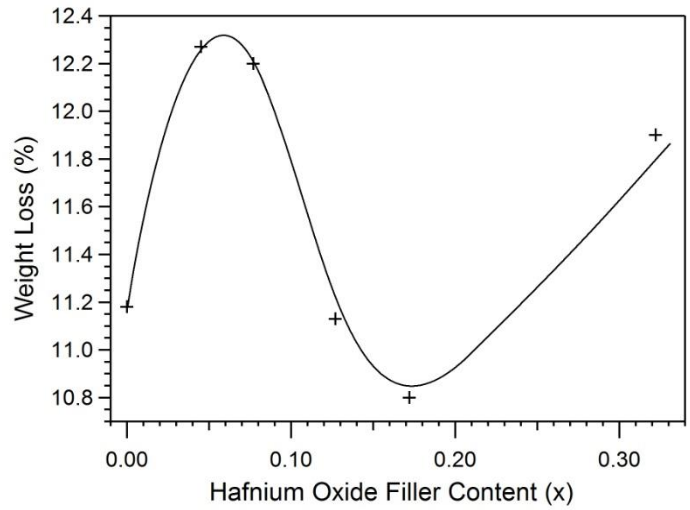

Figure SI-3. Weight loss attributed to acid dehydration with increasing nanofiller content observed by TG analysis

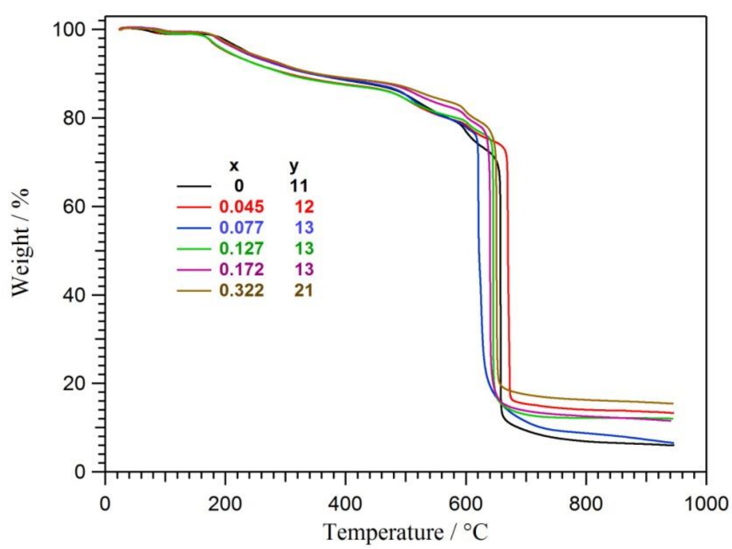

Figure SI-4. TG profiles for $PBI4N(H_3PO_4)_y$ and $[PBI4N(HfO_2)_x](H_3PO_4)_y$ measured under an air atmosphere.

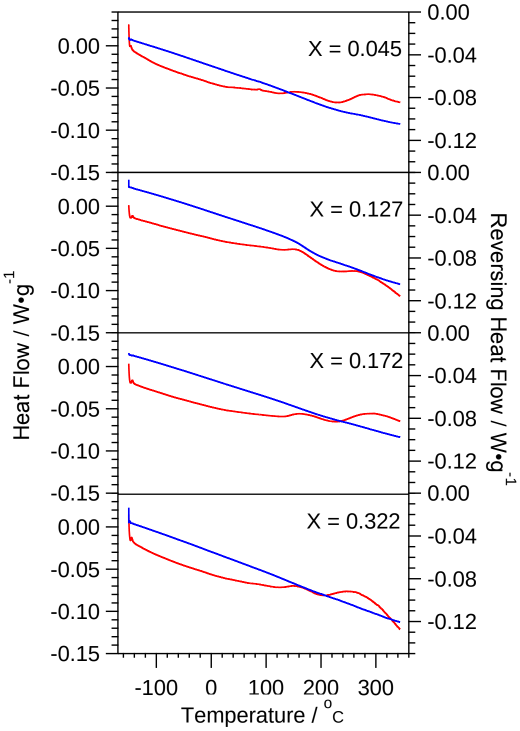

Figure SI-5. MDSC profiles for [PBI4N$(HfO_2)_x$] showing heat flow (red) and reversing heat flow (blue)

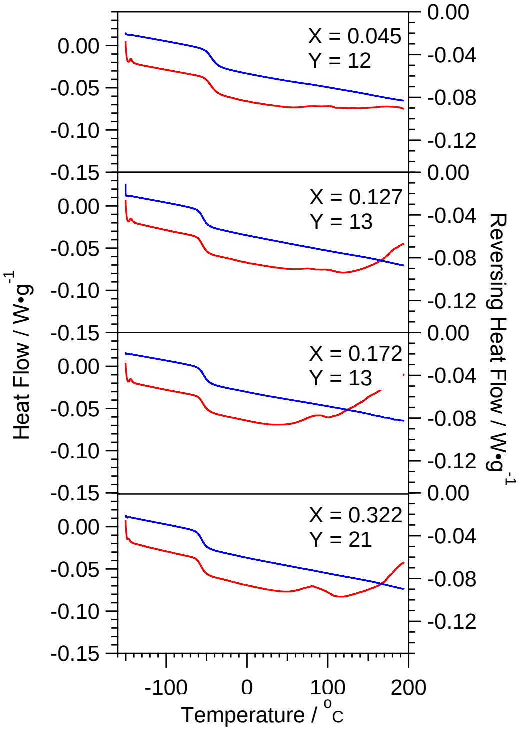

Figure SI-6. MDSC profiles for $[PBI4N(HfO_2)_x](H_3PO_4)_y$ showing heat flow (red) and reversing heat flow (blue)

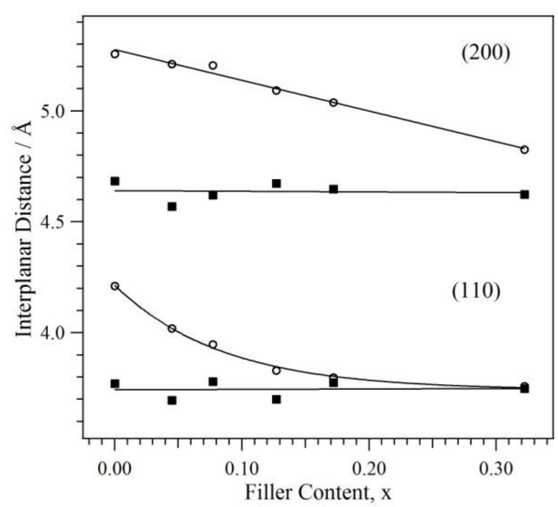

Figure SI-7. The effect of nanofiller content (x) on the interplanar distances of (200) and (110) for undoped (circles) and acid-doped (squares) membranes

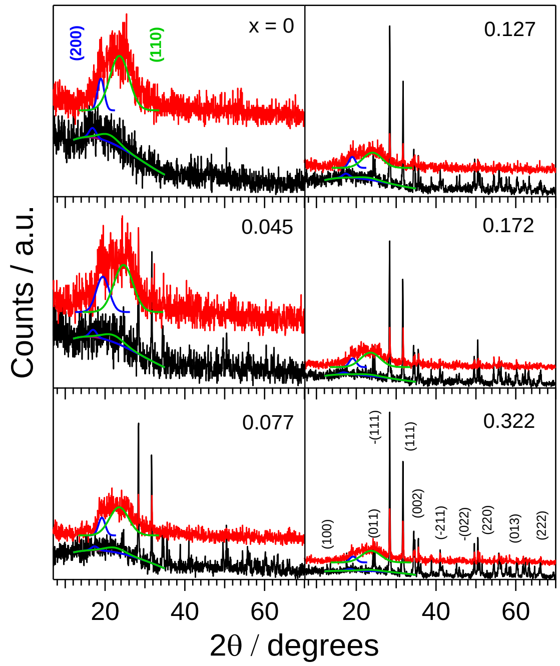

Figure SI-8. WAXS patter of [PBI4N(HfO_2)$_x$] (black) and [PBI4N(HfO_2)$_x$](H_3PO_4)$_y$ (red) with some assigned peaks

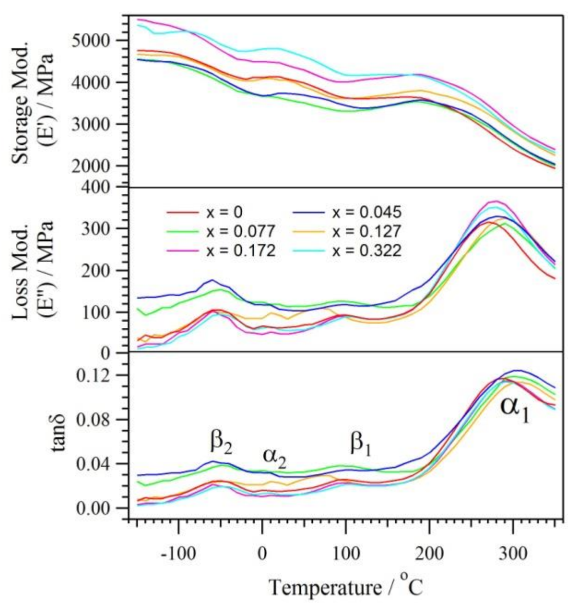

Figure SI-9. Temperature dependent storage modulus (E'), loss modulus (E'') and tan δ profiles for PBI4N and [PBI4N(HfO_2)$_x$]

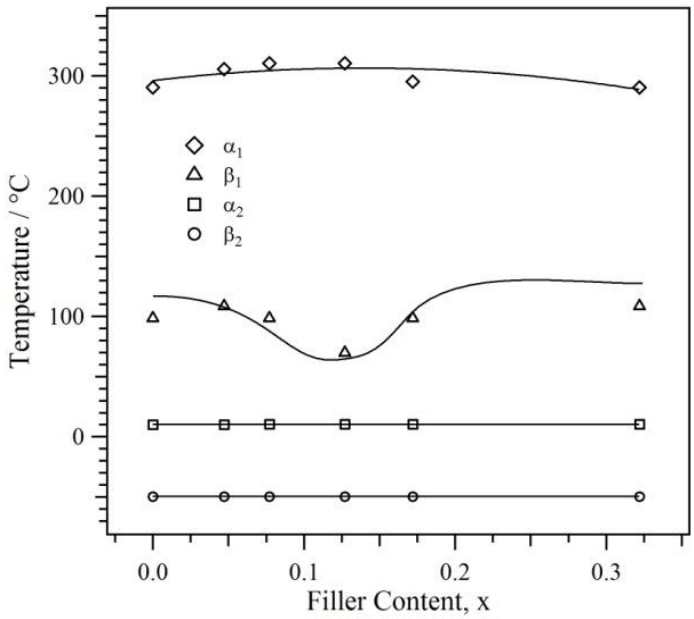

Figure SI-10. Effect of nanofiller content on the 4 mechanical transitions observed by DMA

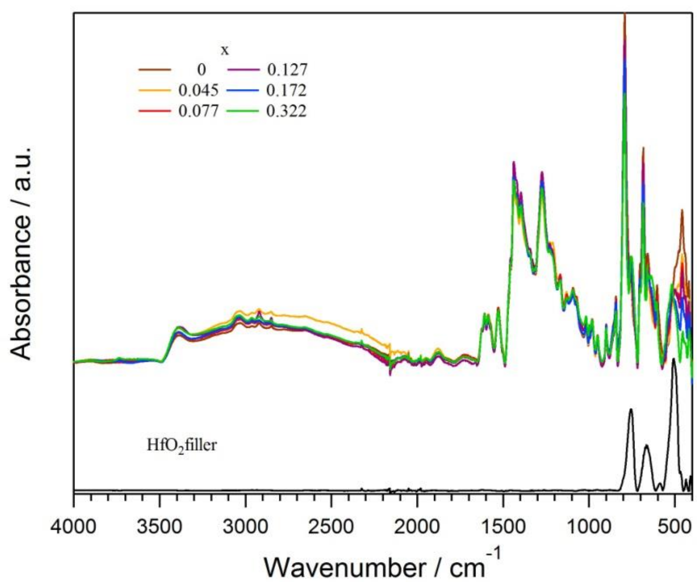

Figure SI-11. FT-IR-ATR spectra of all undoped membranes and neat filler

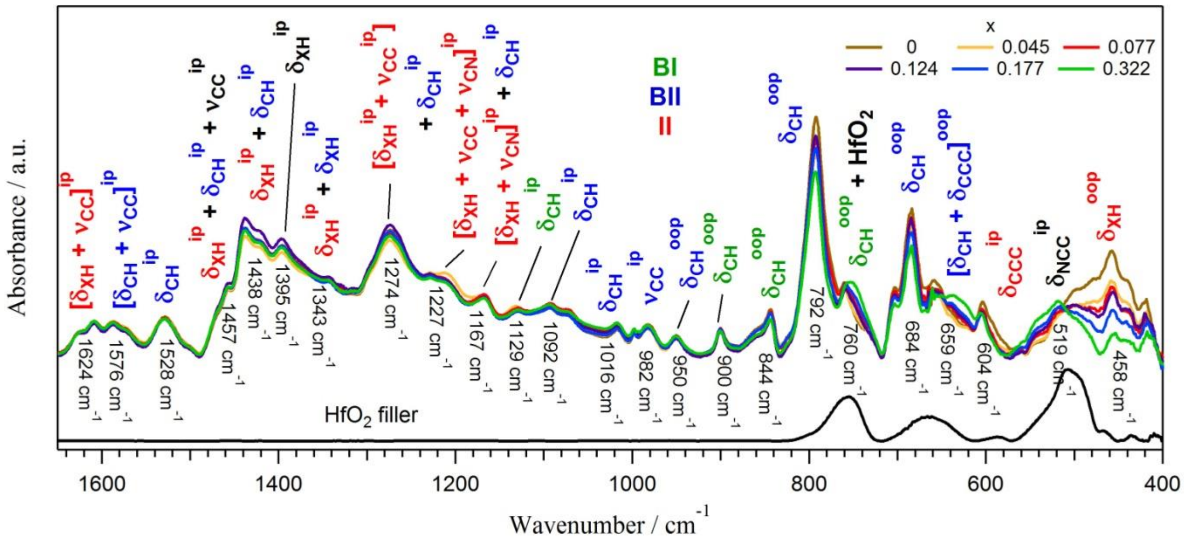

Figure SI-12.FT-IR-ATR spectra of all undoped membranes and neat nanofiller showing assigned in-plane and out-of-plane bands

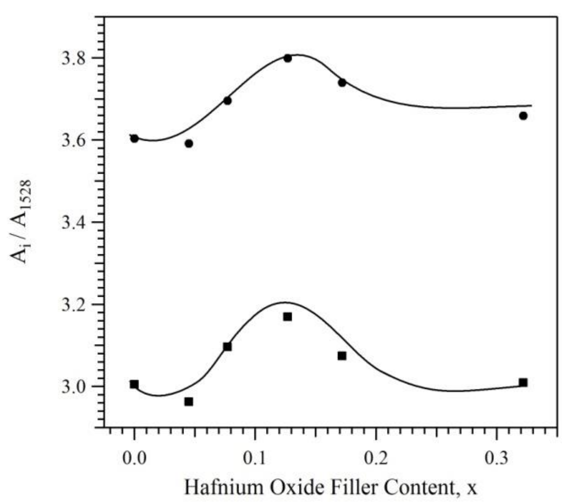

Figure SI-13. Effect of nanofiller levels the on in-plane vibrational bands of [PBI4N(HfO_2)$_x$] occurring at 1439 cm^{-1} (circles) and 1421 cm^{-1} (squares). The areas under the bands are compared with that of the area under the band occurring at 1528 cm^{-1} which is shown to be largely unaffected by nanofiller content

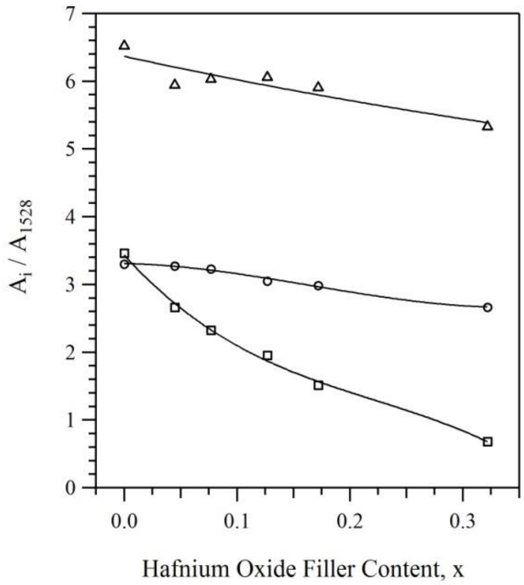

Figure SI-14. Effect of nanofiller levels on the out-of plane bands of [PBI4N(HfO_2)$_x$] occurring at 792 cm^{-1} (triangles) and 684 cm^{-1} (circles) and 458 cm^{-1}(squares). The areas under the bands are compared with that of the area under the band occurring at 1528 cm^{-1} which is shown to be largely unaffected by nanofiller content

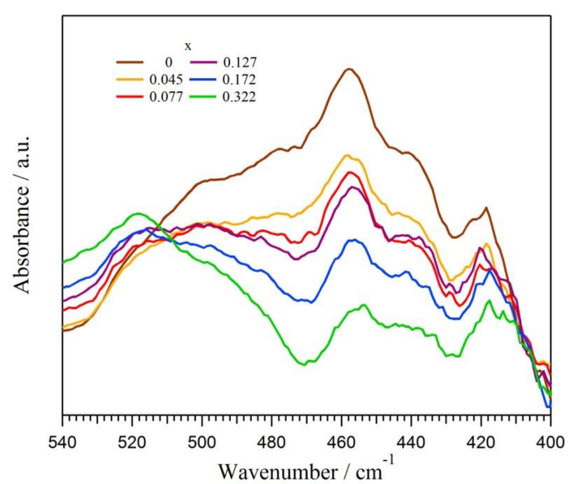

Figure SI-15. FT-IR-ATR spectra of all undoped membranes showing the diminishing intensity of the peak at 458 cm^{-1} with increasing nanofiller content

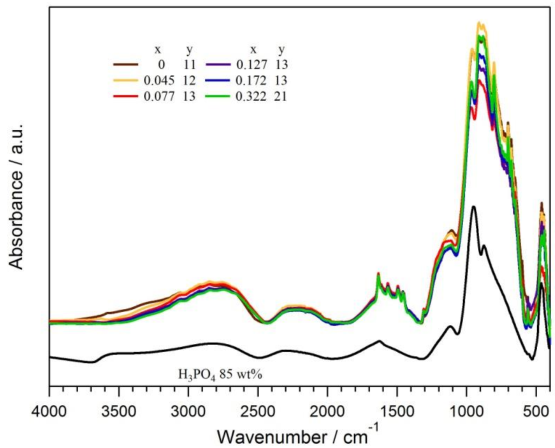

Figure SI-16. FT-IR-ATR spectra of all acid-doped membranes and *o*-phosphoric acid (85 %)

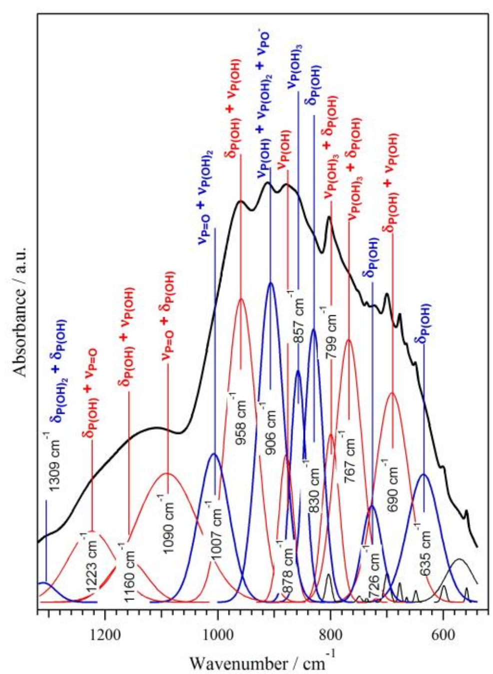

Figure SI-17. Decomposition of the experimental normalized FT-IR-ATR spectra for acid doped PBI4N (black) confirming the presence of H_3PO_4 (red) and $H_2PO_4^-$ (blue)

Figure SI-18. Full FT-IR-ATR assignment of PBI4N$(HfO_2)_x$ and [PBI4N$(HfO_2)_x$]$(H_3PO_4)_y$

[PBI/$(HfO_2)_x$]			**[PBI/$(HfO_2)_x$]/$(H_3PO_4)_y$**		
Observed wavenumber / cm^{-1}	**Calculated wavenumber (Intensity) / cm^{-1} (kJ/mol)**	**Mode description [(a)]**	**Observed wavenumber / cm^{-1}**	**Calculated wavenumber (Intensity) / cm^{-1} (kJ/mol)**	**Mode description [(a)]**
1624 (vw, sh)	1611(49)	$[\delta_{XH}+\nu_{CC}]^{ip}$(II)	1632 (vw)	1599(25)	$[\nu_{CC+}\nu_{CN}+\delta^{ip}{}_{XH}]$(BI+Im)
1608 (vw)	1599(0)	$[\delta_{XH}+\nu_{CC}]^{ip}$(II)	1613 (vw,sh)	1597(89)	$[\nu_{CC+}\nu_{CN}+\delta^{ip}{}_{XH}]$(BI+Im)
1587 (vw)	1581(213)	$[\delta_{CH}+\nu_{CC}]^{ip}$(BII)	1564 (vw)	1557(16)	$[\delta_{CH}+\nu_{CC}]^{ip}$(BII)
1576 (vw, sh)	1559(42)	$[\delta_{CH}+\nu_{CC}]^{ip}$(BII)	1523 (vw)	1523(22)	$\delta^{ip}{}_{NH}+[\nu_{CC}+\delta_{CH}]^{ip}$
1528 (vw)	1517(0.06)	$\delta_{CH}{}^{ip}$(BII)	1494 (vw)	1492(1)	$\delta^{ip}{}_{NH}+[\delta_{CH}+\nu_{CC}+\nu_{CN}]^{ip}$
1457 (vw, sh)	1452(95)	$\delta_{XH}{}^{ip}$(II)$+\delta_{CH}{}^{ip}$(BII)$+\nu_{CC}{}^{ip}$	1483 (vw, sh)	1477(7)	$\delta^{ip}{}_{CH}$(BII)$+\nu^{ip}{}_{CN}$
1438 (m)	1437(0.02)	$\delta_{XH}{}^{ip}$(II)$+\delta_{CH}{}^{ip}$(BII)	1458 (vw)	1459(128)	$[\delta_{XH}+\nu_{CC}+\delta_{CNC}]^{ip}$
			1448 (vw, sh)	1449(7)	$\nu^{ip}{}_{CN}+\delta^{ip}{}_{CH}(BII)+\delta^{ip}{}_{CH}$(BI)
1421 (m, sh)	1421(57)	$\delta_{XH}{}^{ip}$(II)$+\delta_{CH}{}^{ip}$(BII)$+[\nu_{CC}+\nu_{CN}]^{ip}$	1414 (vw)	1407(23)	$\nu^{ip}{}_{CN}+\delta^{ip}{}_{CH}(BII)+\delta^{ip}{}_{CH}$(BI)
1395 (m)	1374(14)	$\delta_{XH}{}^{ip}$(endgroup)	1378 (vw, sh)	1375(11)	$\delta^{ip}{}_{NH}+\delta^{ip}{}_{CH}(BI)+[\nu_{CC}+\delta_{CH}]^{ip}$(BII)
1343 (w)	1348(240)	$\delta_{XH}{}^{ip}$(II+BII)	1343 (vw)	1342(1)	$\delta_{CH}{}^{ip}$(BII)$+\delta^{ip}{}_{XH}$
1274 (m)	1275(33)	$[\delta_{XH}+\nu_{CC}]^{ip}(II)+\delta_{CH}{}^{ip}$(BII)	1309(vw)	1328(4)	$\delta_{P(OH)2}+\delta_{P(OH)}$ $H_{11}P_4O_{16}^-$
1227 (w)	1227(7)	$[\delta_{XH}+\nu_{CC}+\nu_{CN}]^{ip}$(II)	1223 (vw, sh)	1225(361)	$\delta_{(POH)}+\nu_{P=O}$ $[H_3PO_4]_4$ (ε domain probe)

[PBI/(HfO_2)$_x$]			[PBI/(HfO_2)$_x$]/(H_3PO_4)$_y$		
Observed wavenumber / cm^{-1}	**Calculated wavenumber (Intensity) / cm^{-1} (kJ/mol)**	**Mode description (a)**	**Observed wavenumber / cm^{-1}**	**Calculated wavenumber (Intensity) / cm^{-1} (kJ/mol)**	**Mode description (a)**
				1228(200)	$\delta_{P(OH)2}+\delta_{P(OH)}$ $H_{11}P_4O_{16}^-$
1217 (w)	1219(5)	$[\delta_{NH}+\nu_{CN}]^{ip}+\delta_{CH}^{ip}$(BII)	1160 (w)	1159(90)	$\delta_{(POH)}+\nu_{P(OH)}$ $[H_3PO_4]_4$
1167 (w)	1154(0)	$[\delta_{XH}+\nu_{CC}+\nu_{CN}]^{ip}(II)+\delta_{CH}^{ip}$(BII)	1090 (w)	1090(94)	$\delta_{(POH)}+\nu_{P=O}$ $[H_3PO_4]_4$
				1090(297)	$\delta_{P(OH)3}+\delta_{P(OH)2}+\delta_{P(OH)}$ $H_{11}P_4O_{16}^-$
1129 (vw)	1132(12)	δ_{CH}^{ip}(BI)	1007 (w)	989(245)	$\nu_{P=O}+\nu_{P(OH)2}$ $H_{11}P_4O_{16}^-$
1092 (w)	1099(15)	δ_{CH}^{ip}(BII)	958 (vs)	958(204)	$\delta_{POH}+\nu_{P(OH)}$ $[H_3PO_4]_4$
				964(210)	$\delta_{(POH)}+\nu_{P(OH)3}$ $H_{11}P_4O_{16}^-$
				920(272)	$\nu_{P(OH)3}$ $H_{11}P_4O_{16}^-$
1074 (vw)	1073(4)	δ_{CH}^{ip}(BII)$+\delta_{NH}^{ip}$	906 (vs)	881(186)	$\nu_{P(OH)}+\nu_{P(OH)2}+\nu_{PO-}$ $H_{11}P_4O_{16}^-$
1016 (vw)	1004(0.14)	δ_{CH}^{ip}(II)	878 (vs)	883(267)	$\nu_{P(OH)}$ $[H_3PO_4]_4$
				870(113)	$\nu_{P(OH)OO-}+\nu_{P(OH)3}$ $H_{11}P_4O_{16}^-$
998 (vw)		(BII)	857 (vs)	851(221)	$\nu_{P(OH)3}$ $H_{11}P_4O_{16}^-$
982 (vw)	984(1)	ν_{CC}^{ip}(BII)	830	816(213)	δ_{POH} $H_{11}P_4O_{16}^-$
			803	799(32)	δ_{CH}^{oop}(BII)

[PBI/(HfO$_2$)$_x$]			[PBI/(HfO$_2$)$_x$]/(H$_3$PO$_4$)$_y$		
Observed wavenumber / cm^{-1}	**Calculated wavenumber (Intensity) / cm^{-1} (kJ/mol)**	**Mode description [(a)]**	**Observed wavenumber / cm^{-1}**	**Calculated wavenumber (Intensity) / cm^{-1} (kJ/mol)**	**Mode description [(a)]**
950 (vw)	949(5)	$\delta^{oop}{}_{CH}$(BII)	799	793(45)	$\nu_{P(OH)3}+\delta_{POH}$ [H$_3$PO$_4$]$_4$
900 (vw)	916(2)	$\delta^{oop}{}_{CH}$(BI endgroup)	767	767(45)	$\nu_{P(OH)3}+\delta_{POH}$ [H$_3$PO$_4$]$_4$
			749	742(0.09)	$\delta_{NCC}{}^{oop}$
			735	736(1)	$\delta_{CH}{}^{oop}$(BI)+$\delta_{NCC}{}^{oop}$
855 (vw, sh)	856(0.02)	$\delta^{oop}{}_{CH}$(BII)	726	726(26)	δ_{POH} $H_{11}P_4O_{16}^-$
844 (vw)	838(50)	$\delta^{oop}{}_{CH}$(BI)	699 (vw)	705(2)	$\delta_{NCN}{}^{oop}$
792 (vs)	784(7)	$\delta^{oop}{}_{CH}$(BII)	690	694(173)	$\delta_{POH}+\nu_{P(OH)}$ [H$_3$PO$_4$]$_4$
760 (w)	759(5)	$\delta^{oop}{}_{CH}$(BI$_{II}$)	677	680(32)	$\delta_{CH}{}^{oop}$(BII)
			663	664(6)	$\nu^{ip}{}_{ring}$(BII)+$\delta^{oop}{}_{XH}$
750 (vw, sh)	732(0.02)	$\delta^{ip}{}_{CXC}$ *(ring)*	648	639(92)	$\delta^{oop}{}_{NH}$
704 (w)	695(0.32)	$[\delta_{CNC}+\delta_{CCH}]^{oop}$	635	600(36)	δ_{POH} $H_{11}P_4O_{16}^-$
684 (s)	682(54)	$\delta^{oop}{}_{CH}$(BII)			
663 (w, sh)	664(0)	$\nu_{CC}{}^{ip}$(BII+BI) *(ring)*			
659 (w)	656(0)	$[\delta_{CH}+\delta_{CCC}]^{oop}$(BI)			

$[PBI/(HfO_2)_x]$			$[PBI/(HfO_2)_x]/(H_3PO_4)_y$		
Observed wavenumber / cm^{-1}	**Calculated wavenumber (Intensity) / cm^{-1} (kJ/mol)**	**Mode description [a]**	**Observed wavenumber / cm^{-1}**	**Calculated wavenumber (Intensity) / cm^{-1} (kJ/mol)**	**Mode description [a]**
653 (w,sh)	650(3)	$[\delta_{CCC}+\delta_{CNC}]^{ip}$ *(ring)*			
636 (vw, sh)	621(2)	δ^{ip}_{CXC}(endgroup) *(ring)*			
626 (vw, sh)	620(5)	δ^{ip}_{CXC}(endgroup) *(ring)*			
604 (w)	601(0)	$\delta_{CCC}{}^{ip}$(II) *(ring)*	601 (vw)	612(9)	$\delta^{oop}{}_{NH}$
593(vw, sh)	574(1)	$\delta_{CCC}{}^{ip}$(BI+BII) *(ring)*			
546 (vw)	552(49)	$\delta_{NCC}{}^{ip}$ *(ring)*	559 (vw)	558(36)	$\delta^{oop}{}_{XH}$
519 (vw, sh)	517(1)	$\delta_{NCC}{}^{ip}$ *(ring)*			
499 (w)		(BII)	495 (vw, sh)	484(1)	ν_{ring}
478 (w)	468(19)	$\delta^{oop}{}_{CH}$(BII+BI)+$\delta_{CCN}{}^{oop}$(BII+BI)			
458 (m)	459(0)	$\delta^{oop}{}_{XH}$(II)	460 (w)	468(4)	ν_{ring}
441 (w, sh)	434(0)	$\delta_{CCC}{}^{ip}$*(ring rel)*	442 (w)		
418 (w)	411(69)	$\delta^{oop}{}_{NH}$	422 (vw)	424(5)	$[\delta_{CCC}+\delta_{CNC}]^{oop}$